UNIVERSITY OF CALIFORNIA, MERCED

Numerical simulation and phantom experiment of X-ray luminescence computed tomography

A Thesis submitted in partial satisfaction of the requirements for the degree of Master of Science

in

Biological Engineering and Small Scale Technologies (BEST) Graduate Program

by

Kun Zhang

Committee in charge:

Professor Changqing Li, Chair
Professor Kara E. McCloskey
Professor Wei-Chun Chin

The Thesis of Kun Zhang is approved, and is acceptable in quality and form for publication on microfilm and electronically:

Dr. Wei-Chun Chin

Dr. Kara E. McCloskey

Dr. Changqing Li, Chair

University of California, Merced

2015

Acknowledgements

First and foremost, I would like to thank my advisor Dr. Changqing Li, who has enough patience to guide me through every stage of this project and give me detailed help whenever I need. Secondly, I thank Dr. Wei-Chun Chin and Dr. Kara E. McClosky for graciously agree to serve in my committee. Thirdly, I greatly appreciate all the help from the Li Lab members. I would like to thank Dr. Dianwen Zhu for teaching me the reconstruction algorithms, sharing with me his Matlab codes, and providing valuable comments and suggestions to this thesis. I want to express my gratitude for Dr. Wei Zhang for his technical support in conducting the experiments. My thanks are also due to my fellow graduate students Bakijan Rehman and Yue Zhao for sharing project ideas. Finally, I am indebted to my parents who have provided continuous emotional support for my ambition and goals.

Table of Content

List of Tables and Figures

Abstract

X-ray luminescence computed tomography (XLCT) is an emerging hybrid modality in which X-ray excitable particles (phosphor particles) emit optical photons when stimulated with X-ray photons. Optical imaging has high measurement sensitivity but it has limited spatial resolution for deep targets due to high scattering of optical photons. X-ray imaging has high spatial resolution yet its sensitivity is limited. XLCT can potentially combine the high spatial resolution of x-ray imaging with the high sensitivity of optical imaging. In this project, a prototype XLCT imaging system is built, in which a collimated x-ray beam is used to excite x-ray excitable particles. Ultrafine x-ray beams with beam size of about 200 micrometers are used to improve the spatial resolution of XLCT. Numerical simulations and phantom experiments are used to validate the XLCT imaging system. This thesis is outlined as follows:

Chapter 1 presents the overview of XLCT; Chapter 2 presents XLCT system buildup; Chapter 3 describes XLCT reconstruction algorithm and numerical simulation; Chapter 4 reports XLCT phantom experimental results; finally Chapter 5 summarizes the thesis with ideas for future research on XLCT.

Chapter1

XLCT Introduction

1.1 Introduction

In this chapter we will present an overview of X-ray luminescence computed tomography (XLCT). We will compare XLCT with other different molecular imaging modalities, including nuclear imaging and optical imaging. Challenges and problems in XLCT will also be discussed.

1.2 Overview of XLCT system

X-ray luminescence computed tomography (XLCT) is an emerging hybrid modality in which x-ray excitable particles (phosphor particles) emit optical photons when stimulated with X-ray photons [1-6], [53]. Compared with other optical molecular imaging, e.g. bioluminescence tomography (BLT) [7, 8], fluorescence molecular tomography (FMT)[9,10], XLCT has many unique features and strengths. At first, autofluorescence can be avoided, which can improve image sensitivity. Secondly, due to high-energy of x-ray photon used to excite the nanophosphors in tissues, XLCT has the ability to image deep target. Thirdly, XLCT has the potential roles in molecular imaging due to unique combination of capabilities including high sensitivity, specificity, resolution and depth. Lastly, XLCT overcomes the limitations of using radioactive tags on particles (finite time over which particles can be tracked due to half-life, radioactive animals) or fluorescent tags on the surface of these nanoparticles.

During XLCT experiments, a narrow x-ray beam will scan an object based on predefined translational and rotational movements. This method is similar to the first–generation x-ray attenuation CT scanning. An external optical detector will detect emitted optical photons that are emitted by the scintillating contrast agents. The measurement intensity of optical photons can be used to extract the excitable particle density along the x-ray beam. A sinogram of the measurement data is constructed in a way similar to X-ray CT by acquiring measurements at different rotational and translational steps. A typical filtered backprojection (FBP) can be used to reconstruct the cross-section image of nanophosphor distribution.

We anticipate XLCT will be used for biological process non-invasively within living animals at tissue scale instead of organ scale. Moreover, the recent progress of x-ray excitable nanophosphors synthesis [11-13] will make it possible for XLCT to be applied to preclinical and clinical studies.

1.3 Comparison with other molecular imaging modalities

The goal of XLCT is to enable new molecular imaging applications. XLCT and other common tomographic molecular imaging modalities can be compared. Molecular imaging is the imaging of molecular process in living subjects. It is also considered as the combination of the molecular biology and non-invasive in-vivo imaging. Positron emission tomography (PET) using radiolabeled fluoro-dexyglucose (FDG) is the most widespread example of clinical molecular imaging. In this application, PET imaging is used to detect abnormally highly glucose uptake, an important molecular biomarker of cancer. Similarly, XLCT has the potential to be the new imaging tool with which the basic molecular biology underlying disease and other biological process can be studied. In the following section, we will compare nuclear imaging and optical imaging, the two

most commonly used molecular imaging modalities. MRI [32], ultrasound [33], and photoacoustic imaging [34] are also gaining new applications in molecular imaging.

1.3.1 Nuclear imaging

Nuclear imaging including PET and single photon emission computed tomography (SPECT) are the most popular clinical imaging modalities. Nuclear imaging can utilize radio-labeled molecules (radiopharmaceuticals) to evaluate molecular biomarkers in clinical exams. Biochemistry (metabolism, cellular uptake, tissue, and systemic circulation) makes it possible to use radiopharmaceuticals (e.g. FDG), which are synthetic molecules, to probe specific in vivo molecular processes such as glucose uptake. A relatively wide variety of radiopharmaceutical probes offers nuclear imaging a high specificity. The purpose of using the radionuclides in these pharmaceuticals is to emit gamma ray signals that allow imaging system to determine their locations and quantities. Because of a very low gamma radiation signal in tissue background, nuclear imaging methods can have high sensitivity and can detect trace quantities of radiopharmaceuticals. Compared to other modalities, the major drawback of nuclear imaging methods is the relatively low spatial resolution due to the physical limits in focusing and capturing the emitted high-energy gamma rays. The other disadvantages include ionization radiation, high cost of imaging probes, instrumentation and limited half-lives of isotopes.

1.3.2 Optical imaging

Optical imaging modalities (Fluorescence, Bioluminescence, Optical Coherence Tomography and Raman Scattering Tomography) have been the successful molecular imaging tools in basic science and preclinical research. The high sensitivity and non-ionization radiation of optical imaging are the main reasons for their popularity.

On the other hand, whole-body human imaging with optical methods is inconceivable due to the limited penetrating depth of optical photons. Furthermore, due to increasing optical scattering with increasing depth, there is a fundamental trade-off between imaging depth and spatial resolution. The spatial resolution is typically poor in mouse-size subjects. Nevertheless, optical imaging can be used heavily in small-animal imaging studies in which high resolution (at tissue and organ scales) is not required and where imaging depth is not a problem. A variety of chemical and genetic methods in designing optical probes has provided specific imaging of biological processes.

In short, optical imaging modalities have good sensitivity and excellent specificity, but poor imaging depth. Nuclear imaging modalities have excellent sensitivity and imaging depth, but low specificity. It would be ideal to combine the excellent specificity of optical imaging, the high imaging depth of nuclear imaging, and high sensitivity of both methods. It is also desirable to have the high resolution of X-ray absorption imaging. X-ray luminescence computed tomography (XLCT) is such an imaging modality that will have good spatial resolution in tissue with high depth and molecular specificity and sensitivity. We expect that there will be more applications of XLCT for fundamental researches, preclinical and clinical studies.

1.4 Challenges for XLCT

1.4.1 Challenges for image reconstruction

XLCT image reconstruction is to obtain the internal luminescence sources distribution quantitatively. There are many challenges in XLCT reconstruction. The main problem is that XLCT reconstruction is an ill-posed problem, especially for single-view data. The ill-posedness can be worse in case of limited measurement data. To overcome this problem, many simple and effective methods have been proposed to take full advantage of surface measurements. However, with the increasing of measurement, the XLCT weight matrix, which maps the unknown nanophosphor distribution to known measurements, has much larger size. It takes a lot of computational time to form the matrix. One solution of reducing computational time is the compressive technique (CS) [14,15]. Liu [49] first reported a wavelet transform based CS and applied it to optical tomography. The advantage of this method is to make it feasible to use the full set of measurements

In XLCT, the location of the internal luminescence sources is well-determined because of the selective X-ray excitation. However their relative source intensities have uncertainties because of unknown absorption and scattering of the optical photons. A more accurate image reconstruction is needed to minimize optical scattering and absorption.

1.4.2 Challenge for experiment

Another problem in XLCT is the long imaging time, especially with the pencil beam scanning methods. One solution of reducing scanning time is to reduce the number of views. Carpenter et al. took a limited angle tomography to scan a phantom with one beam from only one projection angle but reconstruction tomographic cross sections [17]. Li et al reported two orthogonal projection measurements to implement XLCT reconstruction [18]. Both reconstruction methods use optical scatter and propagation in tissue to localize the emission sources. Reducing the number of X-ray projection view can reduce the imaging system complexity and scanning time.

1.4.3 X-ray excitable nanoparticle problem

The unique feature of XLCT over other X-ray modalities is the use of contrast agent, the X-ray excitable particles, which is critical for XLCT imaging. One important problem is the toxicity of XLCT probes, especially nanophsphors [26]. Although X-ray luminescence molecular imaging has been applied in mice imaging [24], the main obstacle to clinical implementation is the toxicity problem. More details about nanoparticle toxicities have been mentioned in the article [23].

Chapter 2

System Buildup

2.1 Introduction

The current ongoing research of XLCT imaging system is described at first. Then our XLCT imaging system is described, followed by the descriptions of each hardware components in the XLCT imaging system. The function of each hardware and software components are also described in details.

2.2 Ongoing research on XLCT systems

Chen et. al [41] proposes a combined XLCT and CT to obtain quantitative luminescence concentration using the structural information from the X-ray computed tomography in a cone beam XLCT. In order to relieve the severe ill-posedness problem in the cone beam XLT, multi-wavelength measurements are used.

Wang et.al [42] proposes a scanning method utilizing dual-cone beams of X-rays to induce luminescence from nanophosphors and reconstruct the three-dimensional distribution of these particles in a biological sample or small animal. X-rays are focused through a polycapillary lens onto a spot of a few micrometers in size. In order to acquire emission data on an object surface, such X-ray scanning can be point-wise performed. Reliable image reconstruction with high spatial resolution and large imaging depth were obtained from numerical simulation data.

Wang et.al [43] proposed a spectrally-resolving and scattering compensated X-ray luminescence computed tomography (SXLCT) approach to quantify a spatial distribution of nanophosphors within a biological object. In the reconstruction algorithm, X-ray scattering is taken into consideration. A linear relationship is established between the nanophosphor distribution and measured NIR data using the finite element method and inverted using compressive sensing (CS) technique. In the model, x-ray scattering effect, incoherent (Compton scattering) or coherent (Rayleigh scattering), is included in the x-ray photon transport mode [38, 39].

Wang et.al [44] presented x-ray micro-modulated luminescence tomography (XMLT) to quantify a nanophosphor distribution in a thick biological sample with high resolution. The idea was to use a micro-modulated x-ray to locate the distribution of nanophosphors which can have luminescence energy stored for detailed tomographic imaging deeply in tissue samples. In the system prototype, the X-rays can be collimated into a narrow-angle cone-beam to irradiate the Fresnel zone plate which focuses an incoming monochromatic X-ray beam onto focal spot.

Badea et.al [45] built an XLCT system with a dual source micro-CT system. Two novel sampling paradigms resulted in more efficient scanning.

Lei et.al [46] presents limited-angle x-ray luminescence tomography (LAXLT). This method utilized a photon propagation model to enable XLCT for surgical guidance.

Li et.al [47] modeled optical photon propagation in XLCT with diffusion equation and solved it with the finite element method. The preconditioned conjugated gradient (PCG) method is used to minimize the difference between measured and modeled photon intensity and to update XLCT images.

2.3 Overview and Features

Different from the XLCT systems described in the above section, we have built an XLCT imaging system with ultrafine x-ray beam size using small x-ray collimator. The ultrafine x-ray beam scans the object with different translational steps for each rotational projection. The XLCT spatial resolution will be improved with the ultrafine x-ray beam.

The proposed XLCT system includes a computer, a data acquisition box, an X-ray tube, an X-ray power supply unit, a DC power supply unit, a Shad-o-box 1024 X-ray camera, a cooling system, an EMCCD camera, a Labview program and a ShadoCam program. Each of the ten components is described below.

1) X-ray detector (Shad-o-Box 1024 X-Ray camera), is used to detect photon generated by the X-ray tube.

2) ShadoCam program is the X-ray detector control program.

3) X-Ray tube (90873, Oxford Instrument) has tungsten anode and generates X-ray photons with energy up to 50 kVp and current of 2 mA.

4) X-Ray tube power supply unit (Oxford Instrument) provides high voltage for the X-ray tube.

5) DC power supply unit provides power for the X-ray tube.

6) Cooling system is used to cool down the X-ray tube.

7) Labview program is programed in the lab and is used to control and monitor the X-ray tube.

8) Data acquisition box NI 6211(National Instrument) communicates with the X-ray power supply unit.

9) Interlock can automatically shut down the X-ray power when the cabinet door is opened. Interlock is a critical X-ray safety device.

10) EMCCD camera (C9100-13, Hamamatsu) is used to measure the emitted optical photons.

The X-ray tube, X-ray detector and the EMCCD camera are placed inside a large X-ray shielded and optical tight cabinet. Other components including the computer, the power supplies, and the cooling system are placed outside the cabinet.

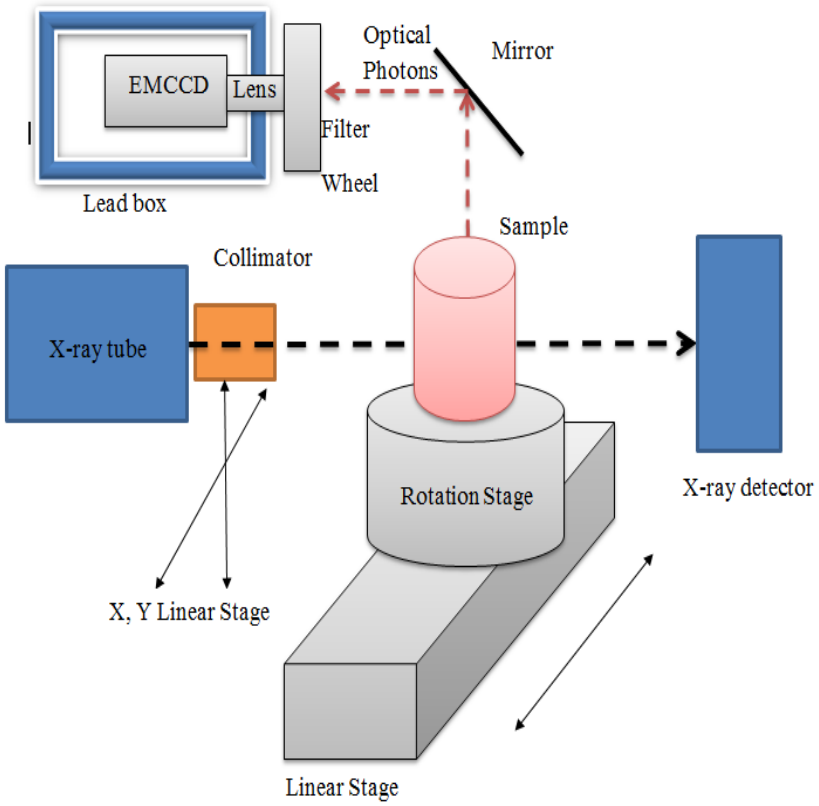
EMCCD
Lens
Optical
Photons
Mirror
Filter
Wheel
Lead box
Sample
Collimator
X-ray tube
Rotation Stage
X-ray detector
X, Y Linear Stage
Linear Stage

(a)

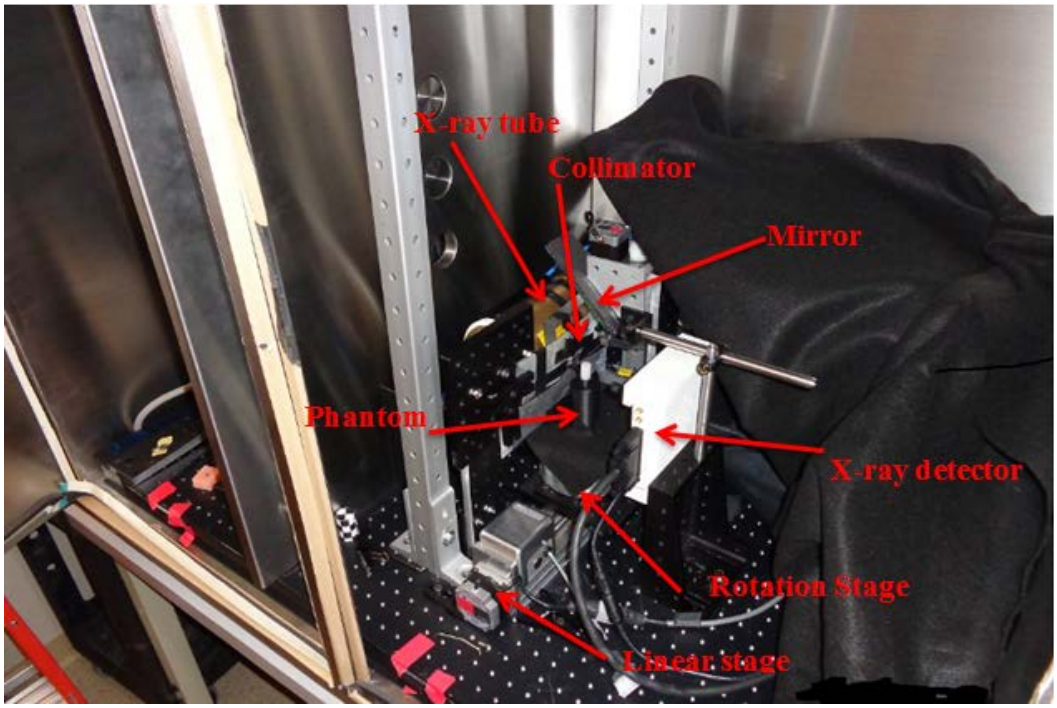
X-ray tube
Collimator
Mirror
Phantom
X-ray detector
Rotation Stage
Linear stage

(b)

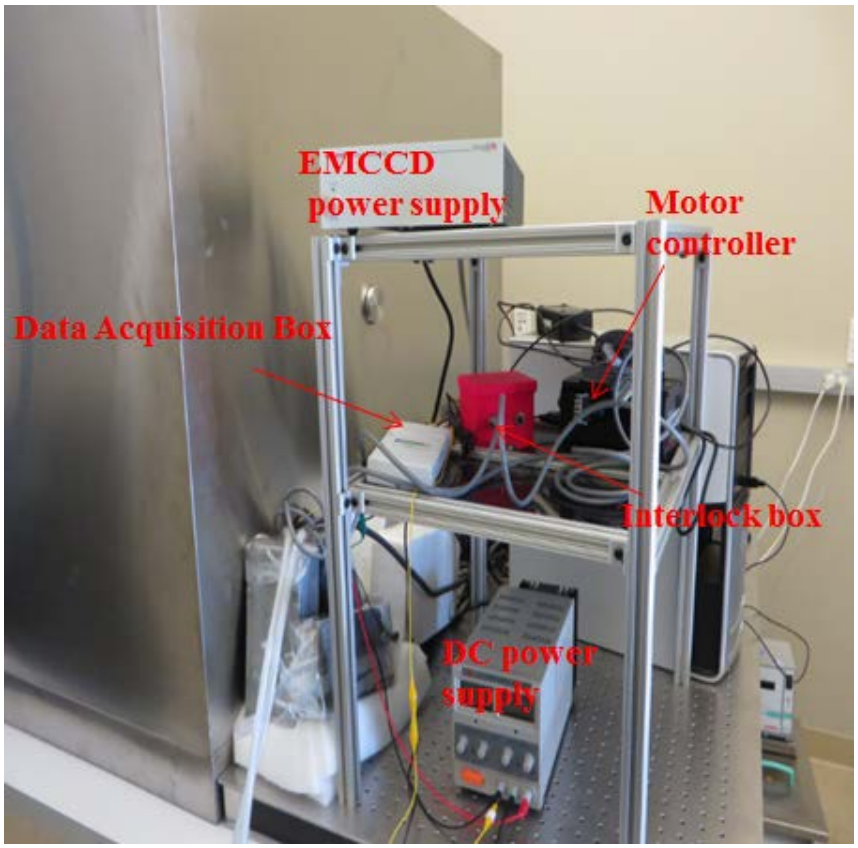

(c)

Figure 1 Schematic (a) and photograph (b, c) of the XLCT imaging system

Fig.1 shows the schematic (a) and photograph (b) (c) of the proposed XLCT imaging system. The hardware contains DC power supply, X-ray power supply, X-ray tube, X-ray detector, data acquisition box, and cooling system. The system contains Labview and ShadoCam software. In this system, DC power supply unit provides voltage and current for X-ray power supply units. X-ray tube emits photons which can be detected by the X-ray detector. Cooling system is used to cool down X-ray tube. A Labview program is used to control voltage and current of X-ray power supply unit through a data acquisition box which communicates between the X-ray power supply unit and the computer through a USB cable. The X-ray tube status is monitored with the Labview program too.

The X-ray tube was controlled to generate X-ray photons up to a maximum energy of 50kVp and tube current of 2 mA. The output X-ray beam was collimated by a 5.08 cm long, 2.54 cm diameter steel rod with a central 100um diameter pin-hole. Phantoms were 3 mm away from the X-ray tube and placed on a motorized rotation stage (B4872TS-ZR, Velmex, Inc.) mounted on a motorized linear stage (MB2509Q1J-S3,Velmex, Inc.).The passed X-ray beam was sensed by an X-ray detector (Shad-o-Box 1024, GOS scintillator screen, Rad-icon Imaging Corporation), which had a detector area

of $49.2 \times 49.2 mm^2$ consisting of a 1024×1024 pixel photodiode array sensor with a 48 um pixel size. The distance from X-ray tube to the detector was 150 mm. The emitted optical photons from the phantom top surface were reflected by a flat mirror and detected by a water-cooled EMCCD camera (C9100-13, Hamamatsu) with a focus lens (f number 1.4, Carl Zeiss). A 1 cm thick lead plated with a circle aperture was placed between the EMCCD camera and the X-ray tube to avoid the influence of high energy X-ray scattering photons. The whole system was fixed on an optical bench and placed in an X-ray shielding and light tight cabinet. All devices during the measurement process were controlled by a program written C++ language in the Visual Studio development environment.

2.3 Hardware and Software Introduction

2.3.1 Hardware Introduction

Figure 2 Photograph of Shad-o-box X-ray detector

Figure 2 shows the image of a X-ray detector (Shad-o-Box 1024,GOS scintillator screen, Rad-icon Imaging corporation, Santa Clara, CA) which has an active detection area of 50mm by 50mm consisting of 1024 by 1024 pixel photodiode array sensor with 48 um pixel spacing. It is a complete detection system for high-resolution imaging. The X-ray detector is controlled by the ShadoCam software and is used to measure the X-ray photon density. The Shad-o-box detector will be mounted inside the imaging system opposite to the X-ray tube.

Figure 3 Photograph of tungsten anode X-ray tube from Oxford Instruments

Figure 3 shows X-ray tube (90873, Oxford Instrument) which has tungsten anode and generates X-ray photons up to 50 kVp with a maximum tube current of 2 mA. The focal spot size is 175 um. The X-ray tube will be mounted on the other side of the imaging system.

Figure 4 Photograph of EMCCD camera

Figure 4 shows EMCCD camera (C9100-13, Hamamatsu) which has great stability, high sensitivity, low noise, and high resolution. This camera provides a full spatial resolution and 16 bits digitization and is used to capture the emitted optical photons on the top surface reflected with a mirror. Bandpass filters are mounted inside the filter wheel to select detected photon wavelengths.

Figure 5 Photograph of data acquisition box NI 6211

Figure 5 shows data acquisition box NI 6211 which has 16 analog inputs and 2 analog outputs. It can provide input and output voltage from -10V to 10V. It communicates between X-ray power supply unit and the computer through a USB cable. We use a Labview program to control the box.

Figure 6 Photograph of VWR heated/refrigerated circulator model 1166

Figure 6 shows VWR heated/refrigerated circulator model (1166) which is used to cool down the X-ray tube. The maximum temperature of X-ray tube is 55 degree centigrade. Water pipe connects between Circulator model and X-ray tube so that it can form a closed cooling system. A flow meter is inserted the cooling system so that water flowing speed is monitored.

Figure 7 Photograph of interlock box

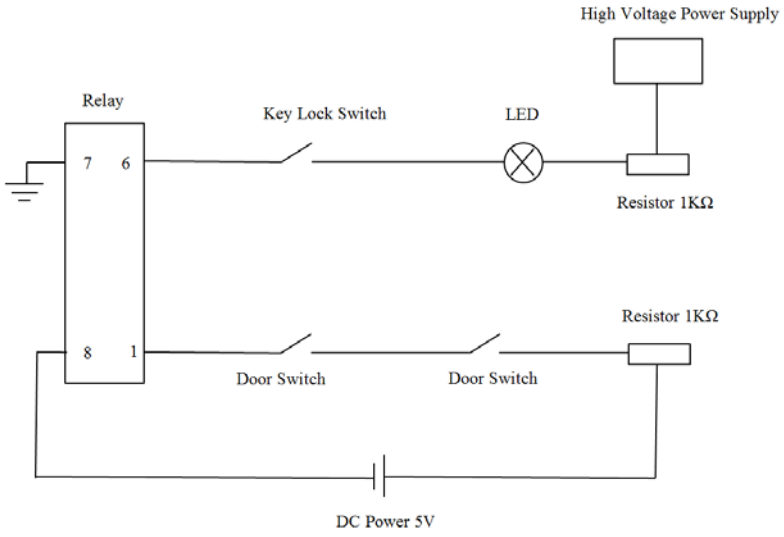

Figure 8 Schematic of interlock system

Figure 7 shows the image of the red color interlock box and figure 8 shows the schematic of the interlock system. The interlock system contains one relay, two magnetic door switches, one key lock switch, two protection resistors, one circuit board and one LED. The circuit board, relay, and protection resistors are in the interlock box. The red color interlock box is designed by AutoCAD and printed by a 3D printer. Two magnetic door switches are attached on both sides of lead shield door. When lead shield doors are

closed, key lock switch is turned on and X-ray power supply is in operation condition and the LED light will be on. Otherwise, LED light will be off and X-ray power supply will be off.

2.3.2 Software Introduction

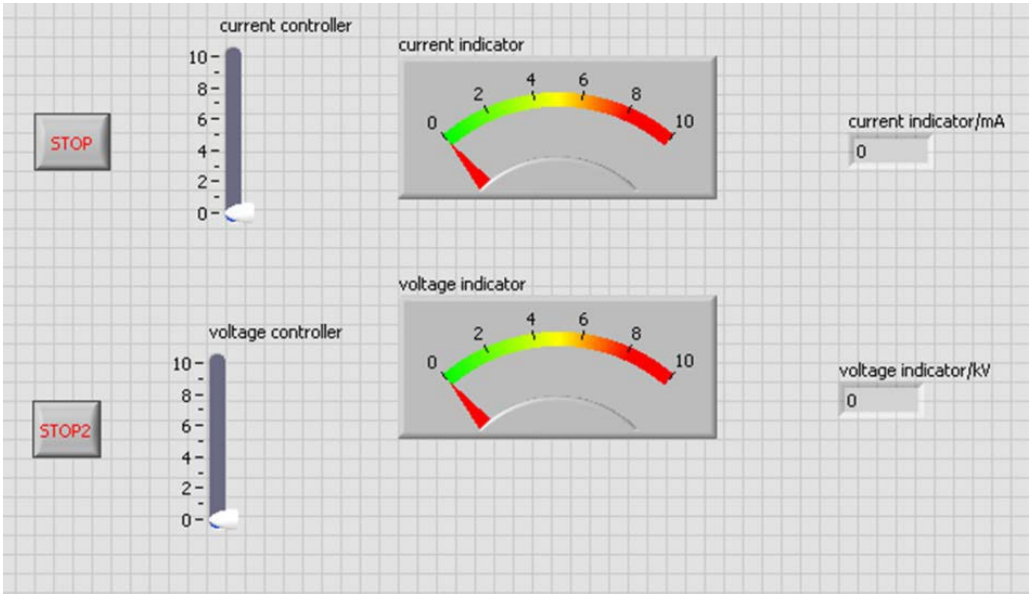

Figure 9 Labview software interface

Figure 9 shows the image of current/voltage controller and current/voltage indicator in Labview interface. Current/voltage controller is used to control current/voltage of x-ray power supply unit. Through the values of voltage and current indicators, the status of X-ray tube is known.

(a)ShadoCam interface when no photons detected

(b)ShadoCam interface when X-ray photons detected

(c)ShadoCam interface when X-ray beam with size of 200um diameter detected

Figure 10 Three measurement pictures at three different conditions in ShadoCam interface

Figure 10 shows three measurement pictures at three different conditions in ShadoCam interface. Fig.10(a) shows that the interface will be black color if no photons detected. Z value in the right bottom side will be less than 50. Fig. 10(b) shows that the ShadoCam interface will be more gray color if more X-ray photons are captured by the X-ray detector. Z value are several thousands. Fig. 10(c) shows ShadoCam interface when x-ray beam with size of 200um diameter detected

Chapter 3

XLCT Simulation and Algorithm

3.1 Introduction

This chapter describes the forward modeling based on continuous wave (CW) diffusion equation for XLCT and the reconstruction based on the majorization-minimization (MM) algorithm. Numerical simulation will also be presented to validate the forward modeling and the reconstruction algorithms.

3.2 Forward modeling for XLCT

We assume that the optical photons amount emitted by phosphor particles within the phantom is proportional to x-ray dose and the particle concentration. The emitted light peak wavelength is at 703nm. We use the diffusion equation to describe the optical photons transportation within the phantoms. The diffuse equation, as described by Eq. (1), is solved by finite element method.

$$\begin{cases} -\nabla \cdot (D(\lambda, \vec{\boldsymbol{r}})\nabla\Phi(\vec{\boldsymbol{r}}) + \mu_a(\lambda, \vec{\boldsymbol{r}})\Phi(\vec{r}) = S_k(\vec{\boldsymbol{r}}) \\ \vec{\boldsymbol{n}} \cdot (D(\lambda, \vec{\boldsymbol{r}})\nabla\Phi(\vec{\boldsymbol{r}}) + C_{Robin}\Phi(\vec{\boldsymbol{r}}) = 0 \end{cases} \tag{1}$$

where $\mu_a(\lambda, \vec{\boldsymbol{r}})$ is the wavelength-dependent absorption at position $\vec{\boldsymbol{r}}$ and $D(\lambda, \vec{\boldsymbol{r}}) = [3\mu_s'(\lambda, \vec{\boldsymbol{r}})]^{-1}$ is the diffusion coefficient with $\mu_s'(\lambda, \vec{\boldsymbol{r}})$ being the reduced scattering coefficient. ∇ is the gradient operator, $\Phi(\vec{\boldsymbol{r}})$ is the emitted near-infrared (NIR) optical photon fluence , $\vec{\boldsymbol{n}}$ is the outer normal vector on the boundary, C_{Robin} is the robin boundary coefficient. $S_k(\vec{\boldsymbol{r}})$ is the k^{th}illumination pattern that can be expressed as

$$S_k(\vec{\boldsymbol{r}}) = \eta T(\vec{\boldsymbol{r}}) x(\vec{\boldsymbol{r}}) \tag{2}$$

η is the phosphor particle NIR light yield, $T(\vec{\boldsymbol{r}})$is the X-ray intensity distribution and $x(\vec{\boldsymbol{r}})$ is the particle concentration to be reconstructed.

Based on the finite element theory, Eq. (1) can be discretized into a matrix equation describe the relationship between the particle concentration and NIR photon fluence at each measurement position

$$A_{n_{d\times I\times J,m}} \cdot x_{m,1} = b_{n_{d\times I\times J,1}} \tag{3}$$

$b_{n_{d\times I\times J,1}}$ is the measurement on the phantom top surface, obtained from the EMCCD camera images.$n_d$is the number of detector nodes on the top surface of the phantom, *I* is the total number of angular projections and the number of linear scan locations for each angular projection is *J*.

$A_{n_{d\times I\times J,m}}$ is the weight matrix can be calculated as

$$A_{n_{d\times I\times J,m}} = \begin{bmatrix} \begin{bmatrix} \vec{\Phi}_1 \otimes \vec{\Gamma}_1 \otimes \vec{\mathrm{T}}_1 \\ \vdots \\ \vec{\Phi}_{n_d} \otimes \vec{\Gamma}_1 \otimes \vec{\mathrm{T}}_1 \end{bmatrix} \\ \vdots \\ \begin{bmatrix} \vec{\Phi}_1 \otimes \vec{\Gamma}_{I\times J} \otimes \vec{\mathrm{T}}_{I\times J} \\ \vdots \\ \vec{\Phi}_{n_d} \otimes \vec{\Gamma}_{I\times J} \otimes \vec{\mathrm{T}}_{I\times J} \end{bmatrix} \end{bmatrix} \tag{4}$$

in which $\otimes$ is the element product of the row vector $\vec{\Phi}_i$, $\vec{\Gamma}_j$ and $\vec{T}_j$ where *i* is from 1 to n_d and *j* is from $I \times J$, *m* is the number of the finite element nodes. $\vec{\Gamma}_j$ (*k* from $I \times J$) is the mask prior constraint vectors expressed as

$$\vec{\Gamma}_k(u) = \begin{cases} 1, when\ the\ node\text{"u" is within the x-ray beam} \\ 0, otherwise \end{cases} \tag{5}$$

where *u* is from 1 to *m*.

3.3 Reconstruction algorithm for XLCT

The typical solution of Eq.(3) is obtained by minimizing the following regularized squared data measurement misfit under the non-negativity constraint

$$\hat{\boldsymbol{x}} = \boldsymbol{argmin}_{\boldsymbol{x},\boldsymbol{x}\geq\boldsymbol{0}}\, \boldsymbol{\mathcal{F}}(\boldsymbol{x}) := \frac{1}{2}\|\boldsymbol{b} - \boldsymbol{A}\boldsymbol{x}\|_2^2 + \alpha\|\boldsymbol{x}\|_p^p \tag{6}$$

where α is the regularization parameters, $\|\boldsymbol{x}\|_p^p$ (p>0) is the L^P norm.

The majorization-minimization(MM) algorithm is applied to solve the optimization problem of Eq (6) . The details of the MM algorithm have been described in [9, 10], [54]. We applied L^1 regularization method in the micro XLCT reconstruction algorithms. The pencil beam X-ray dimensions and location are included in the reconstruction algorithm as priors.

3.4 Numerical Simulation

Case 1: Simulation with target diameter of 1mm

In the numerical simulation, three targets with diameters of 1 mm are embedded in a 12 mm diameter, 40 mm long cylindrical phantom without excitable particle background. The phantom is discretized by a finite element mesh with 21463 nodes, 113968 tetrahedral elements and 14096 face elements. The center positions of targets are at (-1,-2.7321), (0,-1) and (1,-2.7321) so that center-to-center between two targets is 2mm. For each XLCT imaging, the angular step is set at 5, 15, 45 degrees with 36, 12, 4 angular projections, respectively. For each angular projection, the linear stage took 95, 47, and 23 steps with a step size of 0.125mm, 0.25mm, 0.5mm respectively. The X-ray beam size is equal to the step size. For each distinct x-ray beam position, a measurement image corresponding to the optical photon intensity on the phantom top surface is simulated. Finally, 50% of white noise was added to the measurements.

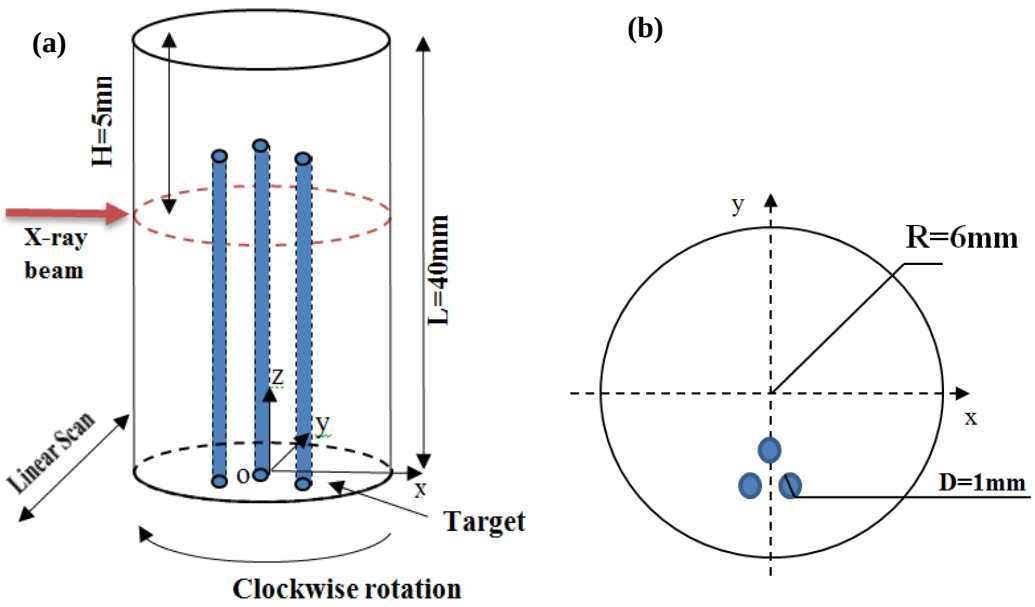

Figure 11 3D geometry of simulation phantom

Figure 11(a) (b) plots 3D geometry of spatial resolution phantom, with three targets of 1 mm diameter. The phantom is scanned at an irradiation depth of 5 mm. The target top surface of the target is 2 mm below the phantom surface.

Figs. 12a, 12b 12c are the reconstructed images with projections of 36, 12 and 4, respectively. A regularization parameter of $1.0e^{-3}$ is used. The beam size is 0.125 mm with 95 linear steps. Figs. 12d, 12e, 12f are the reconstructed image with projections of 36, 12 and 4, respectively. The regularization parameter is $1.0e^{-3}$. The linear scan step is 47 with beam size of 0.25 mm. Figs. 12g, 12h, 12i are the reconstructed image with projections of 36, 12 and 4, respectively. The regularization parameter is $1.0e^{-3}$. The linear scan step is 23 with beam size of 0.5 mm. All of the XLCT images are reconstructed with MM reconstruction algorithm.

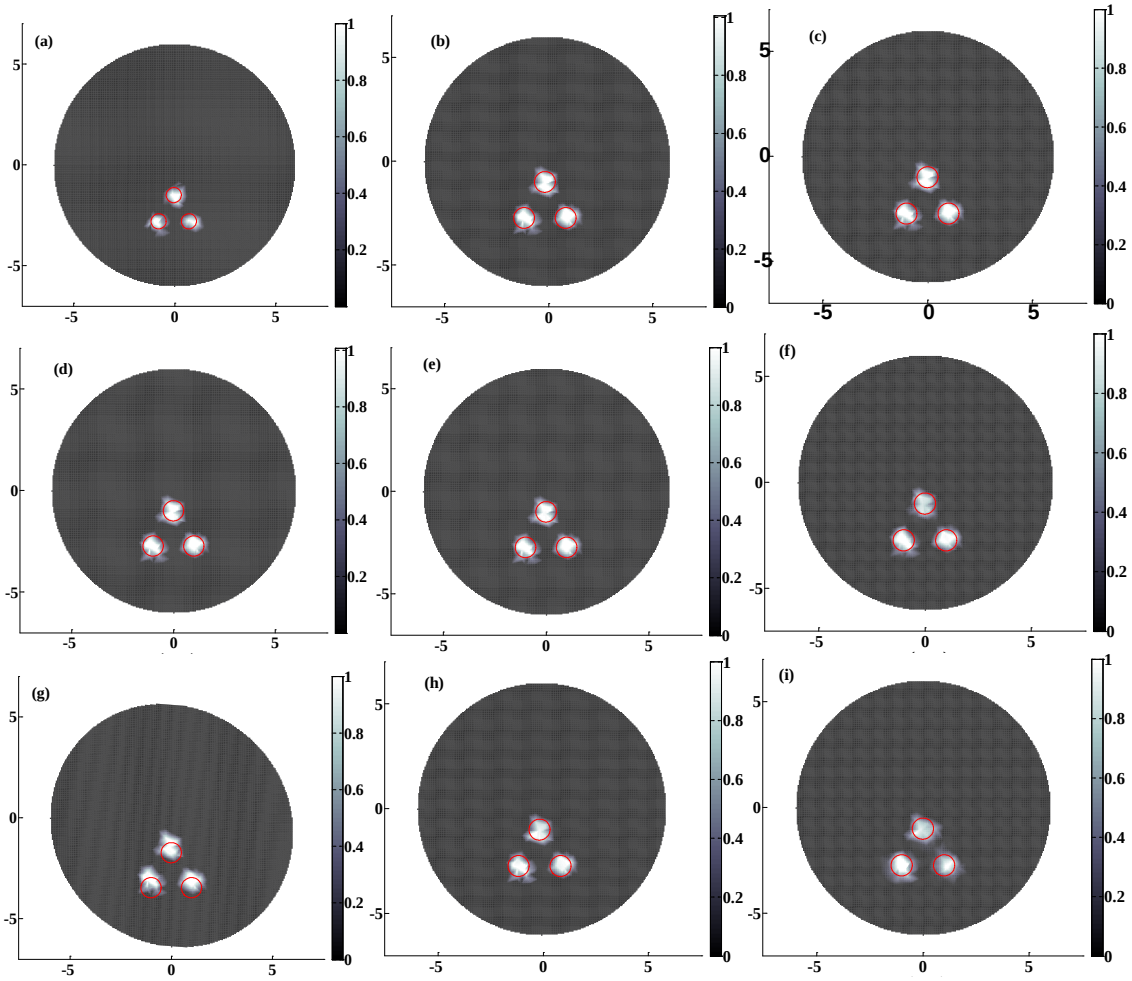

Figure 12 The reconstructed XLCT images with different setup for case 1 (a-i); (a-c) are the reconstructed images with projections of 36, 12 and 4, respectively and regularization parameter of $1.0e^{-3}$ is used. The beam size is 0.125 mm with 95 linear steps; (d-f) are the reconstructed image with projections of 36, 12 and 4, respectively and the regularization parameter is $1.0e^{-3}$. The linear scan step is 47 with beam size of 0.25 mm; (g-i) are the reconstructed image with projections of 36, 12 and 4, respectively and the regularization parameter is $1.0e^{-3}$. The linear scan step is 23 with beam size of 0.5 mm.

We can conclude from the simulation results that the reconstructed image is closer to the ground truth if the number of projections is larger and step size is smaller. We also

find that the targets can be reconstructed successfully even with small measurement projection number of 4.

Case 2: Simulation with target diameter of 0.5 mm

In the numerical simulation, three targets with diameters of 0.5 mm are embedded in a 12 mm diameter, 40 mm long cylindrical phantom without excitable particle background. The phantom is discretized by a finite element mesh with 21463 nodes, 113968 tetrahedral elements and 14096 face elements. Center positions of targets are at (-0.5,-1.866), (0,-1) and (0.5, -1.866) so that center-to-center between two targets is 1mm. For each XLCT imaging, the angular step is set at 5,15,45 degrees with 36,12,4 angular projections, respectively. For each angular projection, the linear stage took 95, 47 and 23 steps with a step size of 0.125mm, 0.25mm, 0.5mm, respectively. The x-ray beam size is equal to the step size. For each distinct x-ray beam position, a measurement image corresponding to the optical photon intensity on the phantom top surface is simulated. Finally, 50% of white noise was added to the measurements.

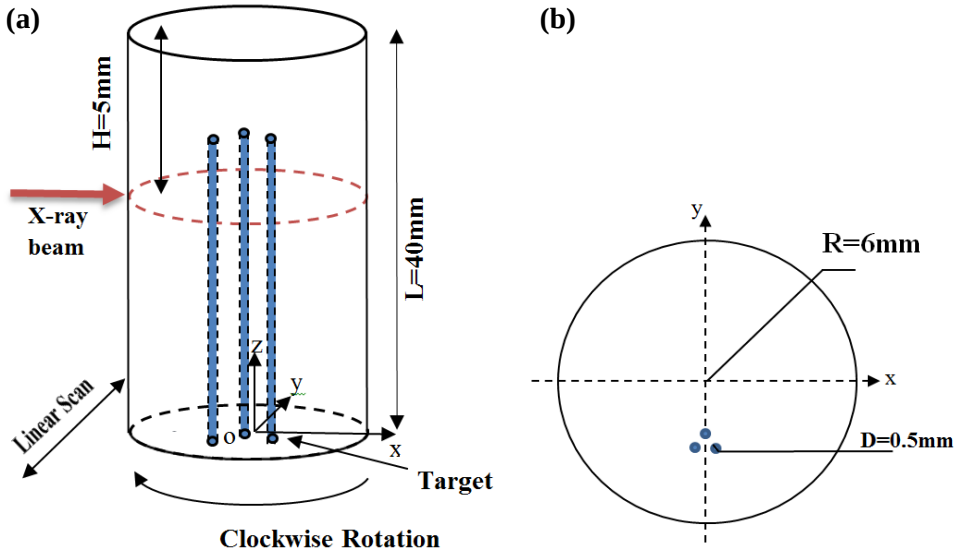

Figure 13 3D geometry of simulation phantom

Figure 13(a) (b) plots 3D geometry of spatial resolution phantom, with three targets of 0.5 mm diameter. The phantom is scanned at an irradiation depth of 5 mm. The target top surface of the target is 2 mm below the phantom surface.

Figs.14a, 14b 14c are the reconstructed images with projections of 36, 12 and 4, respectively. A regularization parameter of $1.0e^{-3}$ is used. The beam size is 0.125 mm with 95 linear steps. Figs.14d, 14e, 14f are the reconstructed image with projections of 36, 12 and 4, respectively. The regularization parameter is $1.0e^{-3}$. The linear scan step is 47 with beam size of 0.25 mm. Figs. 14g, 14h, 14i are the reconstructed image with projections of 36, 12 and 4, respectively. The regularization parameter is $1.0e^{-3}$. The linear scan step is 23 with beam size of 0. 5 mm. All of the XLCT images are reconstructed with MM reconstruction algorithm.

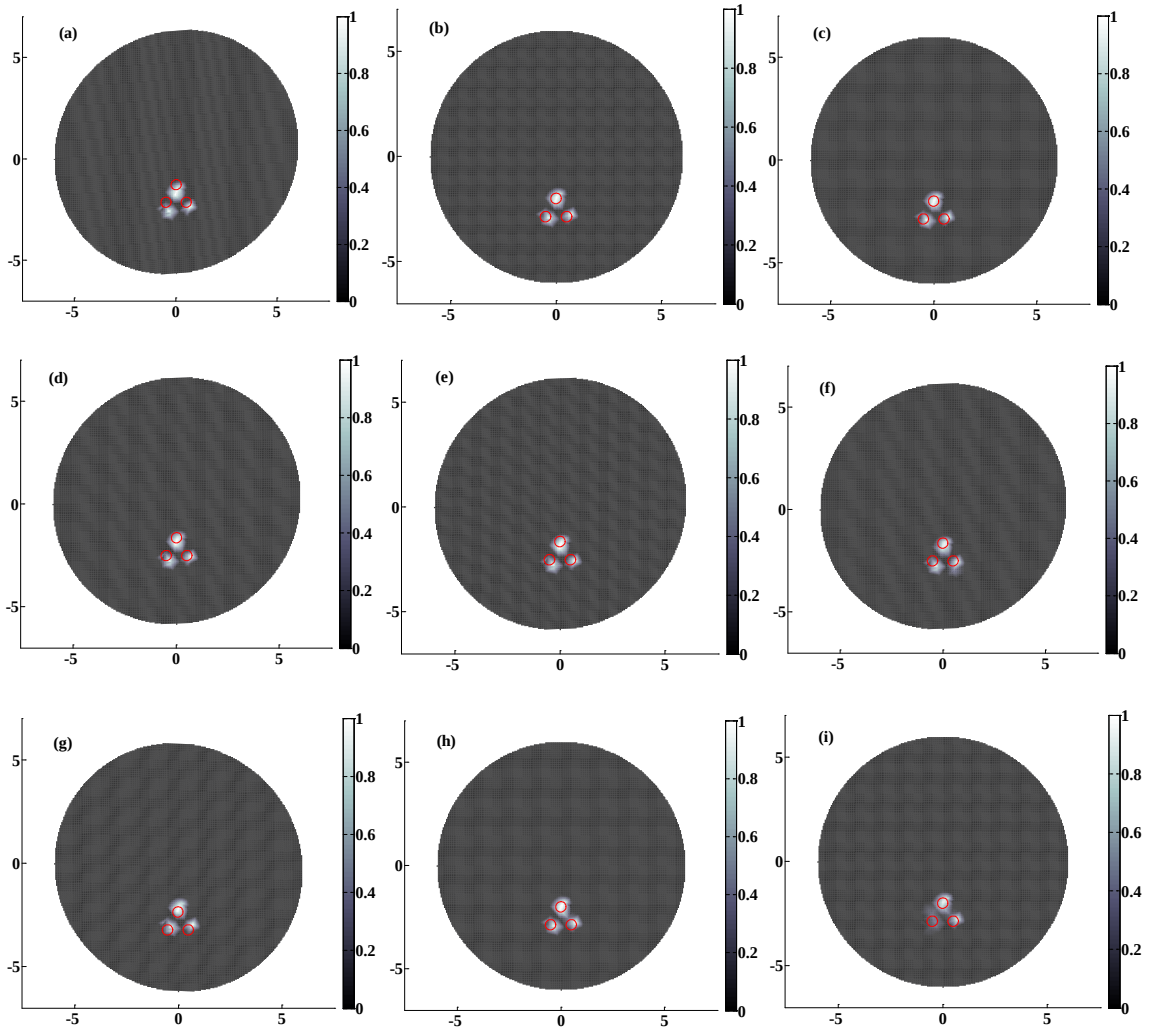

Figure 14 The reconstructed XLCT images with different setup for case 2 (a-i); (a-c) are the reconstructed images with projections of 36, 12 and 4, respectively and regularization parameter of $1.0e^{-3}$ is used. The beam size is 0.125 mm with 95 linear steps; (d-f) are the reconstructed image with projections of 36, 12 and 4, respectively and the regularization parameter is $1.0e^{-3}$. The linear scan step is 47 with beam size of 0.25 mm; (g-i) are the reconstructed image with projections of 36, 12 and 4, respectively. The regularization parameter is $1.0e^{-3}$. The linear scan step is 23 with beam size of 0.5 mm.

We can conclude from the simulation results that the reconstructed image is closer to the ground truth if the number of projections is larger and step size is smaller. We also find that the targets can be reconstructed successfully even with small measurement projection number of 4.

Chapter4

Phantom Experiment Validation

4.1 Introduction

This chapter describes experimental validation of XLCT. The process of making phantom is introduced. The experimental procedure is also described.

4.2 Phantom experiment

One cylindrical phantom (40mm long, 24mm in diameter) composed of 2% agar and 1% intralipid is made to mimic the dimension and optical properties of small animals. One offset small cylinder (38mm long, 4mm in diameter) is embedded as target which is composed of 1 % intralipid, 2% agar and GOS:Eu^{3+} particles (UKL63/UF-R1,Phosphor Technology Ltd.) at the concentration of 10mg/mL and the top surface of the target is 2mm below the phantom surface. Figure 15 shows the phantom geometry and the target off the center. The phantom is scanned at an irradiation depth of 5 mm and XLCT images are reconstructed with measurements of just three angular projections (60 degree apart). The collimated X-ray beam scans the phantoms using 120 linear steps for each projection angle with a step size of 0.2 mm. The spot size of the collimated x-ray beam at the phantom center position is 192 um which is validated by the x-ray detector. During the measurements, the EMCCD camera is water-cooled at -92 º C, the EM gain is set at 240, analog gain is 4, and the exposure time for each x-ray beam scanning position is 8 seconds. The X-ray tube current is 2 mA at 45 kVp.

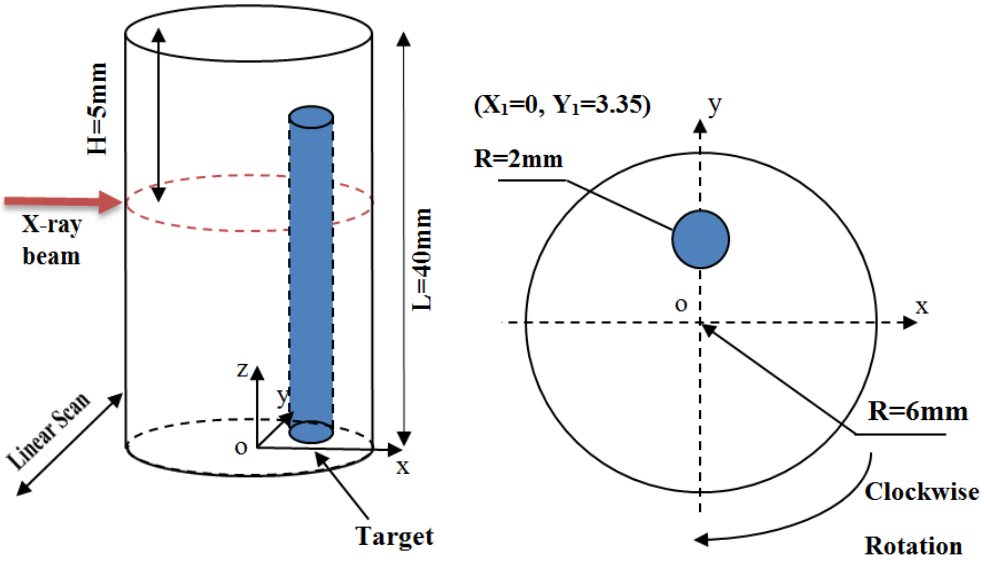

Figure 15 Phantom geometry and scanning scheme

During the image reconstruction process, the phantom was discretized by finite element mesh with 34863 nodes, 184647 tetrahedral elements and 23078 faces. The reconstructed section is discretized with a two dimensional (2D) grid with a pixel size of

200um by 200um. The sensitivity matrix of the 2D grid is interpolated from one sensitivity matrix based on the finite element mesh. The L^1 regularized MM algorithm we studied in numerical simulation was applied here to reconstruct XLCT image. Figure16 displays the reconstructed XLCT image for GOS:Eu^{3+} concentration of 10mg/ml using a 100um diameter collimator, with just three projections. The target is well reconstructed at the correct location. And compared with the former reconstruction results in [52] by using a 1mm diameter collimator, we can find that the image spatial resolution has been dramatically improved without any blur spots around the target region, that is much easier to distinguish the target from the phantom background than before.

We have shown that the small diameter collimator based microXLCT can reach a good spatial resolution. However, small collimator based configuration needs much more scanning positions to cover the entire phantom, which means much more measurement times are needed with current experimental configuration. The X-ray illumination patterns for small collimator based microXLCT system will be optimized with fast measurement, which will be studied in the future.

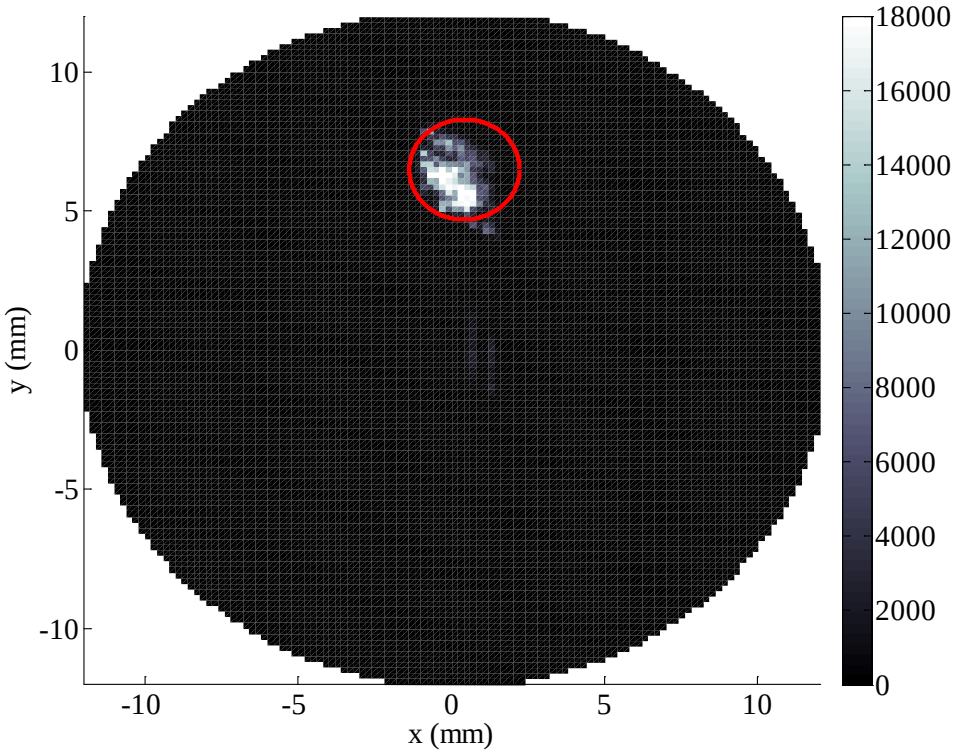

Figure 16 Reconstructed XLCT image for GOS:Eu^{3+} concentration of 10 mg/ml using a 100 μm diameter collimator, with three projection measurements. The red circle indicates the actual target location

4.3 Conclusion

XLCT imaging system has been proposed to detect light from particles that display X-ray luminescence and that are embedded in a phantom. A simultaneous pencil beam CT system is combined into the XLCT system. Measurements using two orthogonal projections are enough to reconstruct an XLCT image.

Chapter 5

Future study plan on XLCT

5.1 Introduction

In this chapter, several topics will be addressed in future research of XLCT.

5.2 Future study plan on XLCT

Several topics need to be addressed in future research of XLCT.

At first, there is still room to improve the XLCT reconstruction accuracy, especially for deep targets. The deeper the target is in the phantom, the larger the reconstruction error. One possible approach is to use new regularization methods and optimization algorithms.

Secondly, the scanning time of XLCT is very long based on current scan plan. Some approaches should be applied to improve the imaging speed. One possible solution is to apply the adaptive scanning method, in which the mouse is scanned at first without collimator to decide the rough location of the target. Then the target zone will be scanned only.

Finally, biocompatible phosphor nanoparticles will be investigated to obtain the x-ray excitable nanophosphors which can be applied to in vivo biomedical studies.

Bibliography & References Cited

[1] G. Pratx, C. M. Carpenter, C. Sun, and L. Xing, "X-ray luminescence computed tomography via selective excitation: a feasibility study," IEEE Trans. Med. Imaging **29**(12), 1992–1999 (2010).

[2] G. Pratx, C. M. Carpenter, C. Sun, R. P. Rao, and L. Xing, "Tomographic molecular imaging of x-ray-excitable nanoparticles," Opt. Lett. **35**(20), 3345–3347 (2010).

[3] C. Li, K. Di, J. Bec, and S. R. Cherry, "X-ray luminescence optical tomography imaging: experimental studies," Opt. Lett. **38**(13), 2339–2341 (2013).

[4] D. Chen, S. Zhu, H. Yi, X. Zhang, D. Chen, J. Liang, and J. Tian, "Cone beam x-ray luminescence computed tomography: A feasibility study," Med. Phys. **40**(3), 031111 (2013).

[5] W. Cong, H. Shen, and G. Wang, "Spectrally resolving and scattering-compensated x-ray luminescence/fluorescence computed tomography," J. Biomed. Opt. **16**(6), 066014 (2011).

[6] X. Liu, Q. Liao, and H. Wang, "In vivo x-ray luminescence tomographic imaging with single-view data," Opt. Lett. **38**(22), 4530–4533 (2013).

[7] G. Wang, W. Cong, K. Durairaj, X. Qian, H. Shen, P. Sinn, E. Hoffman, G. McLennan, and M. Henry, "In vivo mouse studies with bioluminescence tomography," Opt. Express **14**(17), 7801–7809 (2006).

[8] Y. Lv, J. Tian, W. Cong, G. Wang, J. Luo, W. Yang, and H. Li, "A multilevel adaptive finite element algorithm for bioluminescence tomography," Opt. Express **14**(18), 8211–8223 (2006).

[9] V. Ntziachristos, J. Ripoll, L. V. Wang, and R. Weissleder, "Looking and listening to light: the evolution of whole-body photonic imaging," Nat. Biotechnol. **23**(3), 313–320 (2005).

[10] X. Liu, B. Zhang, J. Luo, and J. Bai, "4-D reconstruction for dynamic fluorescence diffuse optical tomography," IEEE Trans. Med. Imaging **31**(11), 2120–2132 (2012).

[11] M. Nichkova, D. Dosev, R. Perron, S. J. Gee, B. D. Hammock, and I. M. Kennedy, "Eu3+-doped Gd2O3nanoparticles as reporters for optical detection and visualization of antibodies patterned by microcontact printing," Anal. Bioanal. Chem. **384**(3), 631–637 (2006).

[12] A. M. Pires, M. F. Santos, M. R. Davolos, and E. B. Stucchi, "The effect of Eu3+ ion doping concentration in Gd2O3 fine spherical particles," J. Alloy. Comp. **344**(1-2), 276–279 (2002).

[13] R. Bazzi, M. A. Flores-Gonzalez, C. Louis, K. Lebbou, C. Dujardin, A. Brenier, W. Zhang, O. Tillement, E. Bernstein, and P. Perriatc, "Synthesis and luminescent properties of sub-5-nm lanthanide oxides nanoparticles," J. Lumin. **102–103**, 445–450 (2003).

[14] T. J. Rudge, V. Y. Soloviev, and S. R. Arridge, "Fast image reconstruction in fluorescence optical tomography using data compression," Opt. Lett. **35**(5), 763–765 (2010).

[15] N. Ducros, C. D'andrea, G. Valentini, T. Rudge, S. Arridge, and A. Bassi, "Full-wavelet approach for fluorescence diffuse optical tomography with structured illumination," Opt. Lett. **35**(21), 3676–3678 (2010).

[16] Xing MM, Cao WH, Pang T, Ling XQ, Chen N. Preparation and characterization of monodisperse spherical particles of X-ray nano-phosphors based on Gd2O2S:Tb. Chinese Science Bulletin. 2009;54(17):2982-6.

[17] C. M. Carpenter, G. Pratx, C. Sun, and L. Xing, ``Limited-angle X-ray luminescence tomography: Methodology and feasibility study," *Phys. Med. Biol.*, vol. 56, no. 12, pp. 3487_3502, Jun. 2011.

[18] C. Li, K. Di, J. Bec, and S. R. Cherry, ``X-ray luminescence optical tomography imaging: Experimental studies," *Opt. Lett.*, vol. 38, no. 13, pp. 2339_2341, Jul. 2013.

[19] J. R. Singer, F. A. Grünbaum, P. Kohn, and J. P. Zubelli, ``Image reconstruction of the interior of bodies that diffuse radiation," *Science*, vol. 248, no. 4958, pp. 990_993, May 1990.

[20] S. R. Arridge, P. van der Zee, M. Cope, and D. T. Delpy, ``Reconstruction methods for infrared absorption imaging," *Proc. SPIE, Time-Resolved Spectrosc. Imag. Tissues*, vol. 1431,pp. 204_215, May 1991.

[21] M. A. O'Leary, D. A. Boas, B. Chance, and A. G. Yodh, ``Experimental images of heterogeneous turbid media by frequency-domain diffusingphoton tomography," *Opt. Lett.*, vol. 20, no. 5, pp. 426_428, Mar. 1995.

[22] B.W. Pogue, M. S. Patterson, H. Jiang, and K. D. Paulsen, ``Initial assessment of a simple system for frequency domain diffuse optical tomography," *Phys. Med. Biol.*, vol. 40, no. 10, pp. 1709_1729, Oct. 1995.

[23] A. Nel, T. Xia, L. Mädler, and N. Li, ``Toxic potential of materials at the nano level," *Science*, vol. 311, no. 5761, pp. 622_627, Feb. 2006.

[24] X. Liu, Q. Liao, and H. Wang, ``*In vivo* X-ray luminescence tomographic imaging with single-view data," *Opt. Lett.*, vol. 38, no. 22, pp. 4530_4533, Nov. 2013.

[25] Tian Y, Cao WH, Luo XX, Fu Y. Preparation and luminescence property of Gd2O2S : Tb X-ray nano phosphors using the complex precipitation method. Journal of Alloys and Compounds 007;433:313-7.

[26] L. Xiong, T. Yang, Y. Yang, C. Xu, and F. Li, ``Long-term in vivo biodistribution imaging and toxicity of polyacrylic acid-coated upconversion nanophosphors," *Biomaterials*, vol. 31, no. 27, pp. 7078_7085, Sep. 2010.

[27] A. M. Derfus, W. C. W. Chan, and S. N. Bhatia, ``Probing the cytotoxicity of semiconductor quantum dots," *Nano Lett.*, vol. 4, no. 1, pp. 11_18, Jan. 2004.

[28] H. S. Choi *et al.*, ``Renal clearance of quantum dots," *Nature Biotechnol.*, vol. 25, no. 10, pp. 1165_1170, Oct. 2007.

[29] Wang SZ, Jarrett BR, Kauzlarich SM, Louie AY. Core/shell quantum dots with high relaxivity and photoluminescence for multimodality imaging. J Am Chem Soc. 2007;129(13):3848-56.

[30] Zavattini G, Vecchi S, Mitchell G, Weisser U, Leahy RM, Pichler BJ, et al. A hyperspectral fluorescence system for 3D in vivo optical imaging. Physics in Medicine and Biology. 2006;51(8):2029-

[31] W. Cong, C.Wang, and G.Wang. (Sep. 2013). ``Stored luminescence computed tomography." [Online]. Available: http://arxiv.org/abs/1309.3585

[32] R. Weissleder *et al.*, ``*In vivo* magnetic resonance imaging of transgene expression," *Nature Med.*, vol. 6, no. 3, pp. 351_355, Mar. 2000.

[33] B. A. Kaufmann and J. R. Lindner, ``Molecular imaging with targeted contrast ultrasound," *Current Opinion Biotechnol.*, vol. 18, no. 1, pp. 11_16, Feb. 2007.

[34] H. F. Zhang, K. Maslov, G. Stoica, and L. V. Wang, ``Functional photoacoustic microscopy for high-resolution and noninvasive *in vivo* imaging," *Nature Biotechnol.*, vol. 24, no. 7, pp. 848_851, Jul. 2006.

[35] Y. Ye, H. Yu, Y. Wei, and G. Wang, "A general local reconstruction approach on a truncated Hilbert transform," *Int. J. Biomed. Imaging* **2007**, 63634 (2007).

[36] H. Yu and G.Wang, "Compressive sensing based interior tomography," *Phys. Med. Biol.* **54**, 2791–2805 (2009).

[37] J. Yang, H. Yu, M. Jiang, and G. Wang, "High-order total variation minimization for interior tomography," *Inverse Problems* **26**, 035013 (2010).

[38] J. Als-Nielsen and D. McMorrow, *Elements of Modern X-ray Physics*, Wiley, New York 2001.

[39] J. H. Hubbell,W. J.Veigele, E. A. Briggs,R.T.Brown,D.T.Cromer, and R. J. Howerton, "Atomic form factors, incoherent scattering functions,and photon scattering cross sections,"*J. Phys. Chem. Ref. Data* **4**, 471–538 (1975).

[40] Gordon R. Stop Breast Cancer Now! Imagining Imaging Pathways Toward Search, Destroy, Cure, and Watchful Waiting of Premetastasis Breast Cancer. Breast Cancer. 2011:167–203.

[41] D. Chen, S. Zhu, X. Chen et al "Quantitative cone beam X-ray luminescence tomography/X-ray computed tomography imaging" Applied Physics Letters 105, 191104 (2014); doi: 10.1063/1.4901436

[42] W. Cong, Z. Pan, R. Filkins, A. Srivastava,N. Ishaque,P. Stefanov, and G. Wang, "X-ray micromodulated luminescence tomography in dual-cone geometry", Journal of Biomedical Optics 19(7), 076002 (July 2014)

[43] W. Cong, H. Shen, and G. Wang, **"**Spectrally resolving and scattering compensated x-ray luminescence/fluorescence computed tomography", Journal of Biomedical Optics 16(6), 066014 (June 2011)

[44] W. Cong, F. Liu, C. Wang, and G. Wang, "X-ray micro-modulated luminescence tomography (XMLT)" OPTICS EXPRESS 5572

[45] C.T. Badea, I.N. Stanton, S.M. Johnston, G.A. Johnson, and M.J. Therien. "Investigations on X-ray luminescence CT for small animal imaging" Proc SPIE. 2012 ; 8313: 83130T.

[46] C M Carpenter, G Pratx, C Sun and L Xing "Limited-angle x-ray luminescence tomography: methodology and feasibility study" Phys. Med. Biol. **56** (2011) 3487–3502

[47] C. Li, Arnulfo Martínez-Dávalos, and S. Cherry "Numerical simulation of x-ray luminescence optical tomography for small-animal imaging" Journal of Biomedical Optics 19(4), 046002 (April 2014)

[48] Vardi Y, Shepp LA, Kaufman L. A Statistical-Model for Positron Emission Tomography. Journal of the American Statistical Association. 1985; 80(389):8–20.

[49] X. Liu, H. Wang, M. Xu, S. Nie, and H. Lu "A wavelet-based single-view reconstruction approach for cone beam x-ray luminescence tomography imaging", 1 November 2014 | Vol. 5, No. 11 | DOI:10.1364/BOE.5.003848 | BIOMEDICAL OPTICS EXPRESS 3848

[50] Y. Ye, H. Yu, Y. Wei, and G. Wang, "A general local reconstruction approach on a truncated Hilbert transform," *Int. J. Biomed. Imaging* **2007**, 63634 (2007).

[51] J. Yang, H. Yu, M. Jiang, and G. Wang, "High-order total variation minimization for interior tomography," *Inverse Problems* **26**, 035013 (2010).

[52] Li, C., Di, K., Bec, J. and Cherry, S. R., "X-ray luminescence optical tomography imaging: experimental studies," Opt. Lett. 38(13), 2339-2341 (2013).
[53] W Zhang, D Zhu, K Zhang, C Li “Microscopic x-ray luminescence computed tomography” SPIE BiOS, 2015
[54] D Zhu, C Li “Nonconvex regularizations in fluorescence molecular tomography for sparsity enhancement” 2014 Phys. Med. Biol. 59 2901.